https://doi.org/10.30799/jnst.S101.26110201 J. Nanosci. Tech. - Volume 11 Issue 2 (2026) 1040–1044

Share Your Innovations through JACS Directory

Journal of Nanoscience and Technology

Visit Journal at https://www.jacsdirectory.com/jnst

ISSN: 2455-0191

# Synthesis and Characterization of Nickel Ferrite ($NiFe_2O_4$) Nanoparticles Through Co-Precipitation Method

Sharada Navnath Adik*

*Department of Physics, Mula Education Society's Shri. Dnyneshwar Mahavidyalay, Newasa, Ahilyanagar – 414 603, Maharashtra, India.*

ARTICLEDETAILS

*Article history:*
Received 27 January 2026
Accepted 16 February 2026
Available online 08 March 2026

*Keywords:*
Nickel Ferrite
Thermal Calcination
Urbach Energy
Spinel Ferrites

ABSTRACT

A promising class of ferrimagnetic materials, nickel ferrite ($NiFe_2O_4$) nanoparticles have great potential for use in microwave devices, magnetic storage systems, catalysis, and biomedical applications such as targeted drug administration. This study offers a thorough analysis of $NiFe_2O_4$ nanoparticles produced by co-precipitation, including a thorough assessment of both as-prepared and thermally treated (600 °C) samples. Under regulated conditions (pH 10.13 ± 0.06, reaction temperature of 80 °C), the synthesis used a stoichiometric $Ni^{2+}$:$Fe^{3+}$ molar ratio of 1:2. An inverse spinel cubic structure with crystallite diameters of 6.50 nm (as-prepared) and 7.14 nm (calcined at 600 °C), indicating a 9.8% increase after thermal treatment, was validated by structural characterisation using powder X-ray diffraction. Because of particle sintering and agglomeration, calcination increased crystallinity from 70.0% to 73.9% while decreasing specific surface area by 10.3% (from 174 to 156 $m^2/g$). A limited, concentrated size distribution (mean 9.0 nm, 70% within the 7-11 nm range) was shown by scanning electron microscopy study of 200 nanoparticles, indicating good nucleation and growth control. Following calcination, optical characterisation using diffuse reflectance spectroscopy showed a notable 20% decrease in Urbach energy (0.30 to 0.24 eV) and a 3.4% rise in band gap energy (1.76 to 1.82 eV), indicating significantly reduced electronic disorder and enhanced crystalline quality. The XRD crystallite size (6.5-7.14 nm) was significantly smaller than the SEM particle diameter (9.0 nm), indicating that the particles are aggregates of mesoporous primary crystallites. The co-precipitation protocol's dependability and scalability were confirmed by a thorough batch-to-batch reproducibility analysis that showed remarkable consistency in product output (82.27 ± 0.83%, coefficient of variation = 1.0%). These results demonstrate the effectiveness and reproducibility of co-precipitation in the production of high-quality $NiFe_2O_4$ nanoparticles with tunable characteristics, offering quantitative direction for thermal parameter optimization for particular applications.

## 1. Introduction

Spinel ferrites represent an important class of magnetic ceramic materials with the general formula $MFe_2O_4$, where M is a divalent transition metal cation ($Ni^{2+}$, $Zn^{2+}$, $Mn^{2+}$, $Cu^{2+}$, etc.) [1, 2]. In particular, nickel ferrite ($NiFe_2O_4$) has an inverse spinel cubic structure where $Ni^{2+}$ and $Fe^{3+}$ ions disperse among octahedral B-sites and $Fe^{3+}$ ions primarily occupy tetrahedral A-sites. $NiFe_2O_4$ has special ferrimagnetic properties due to this structural arrangement, which makes it useful for use in microwave devices, solid oxide fuel cells, magnetic storage systems, catalysis, and targeted drug administration.

Reducing particle size to the nanoscale scale significantly improves the surface-area-to-volume ratio, increasing reactivity, catalytic activity, and magnetic responsiveness, as recent developments in nanomaterials research have shown. Nevertheless, it is still technically difficult to create nanocrystalline $NiFe_2O_4$ with precise size distributions, high purity, and repeatable physicochemical characteristics. Co-precipitation stands out as a particularly useful and scalable method among the available synthesis routes, such as sol-gel combustion, hydrothermal treatment, and microemulsion techniques, because of its ease of use, affordability, and ability to create uniform nanoparticles with controlled morphology [3, 4].

In co-precipitation, metal salt precursors dispersed in aqueous solution are uniformly nucleated and precipitated by using a base to control pH. The desired oxide phase is then obtained by drying and calcining the mixture. One crucial stage in the optimization of nanomaterials is post-synthesis calcination. High-temperature thermal treatment can lower defect concentrations, increase long-range crystallographic order, and encourage crystallite development, all of which have an impact on optical, magnetic, and catalytic properties. According to earlier research on metal oxide nanoparticles, calcination typically improves crystallite size and crystallinity at the price of specific surface area because to agglomeration and necking. Through mechanisms including changes in particle size, defect concentration, and electronic structure, thermal treatment may cause minor alterations in band gap energy and Urbach energy (a measure of disorder-related band-tail states) for optical characteristics [5, 6].

Although co-precipitation is widely used for $NiFe_2O_4$ synthesis, there are still few thorough characterization studies in the literature that systematically compare as-prepared and calcined samples across a variety of parameters, such as X-ray crystallography, surface area analysis, optical properties, and particle morphology. Furthermore, although it is sometimes disregarded, quantitative evaluation of batch-to-batch synthesis repeatability is crucial for creating dependable production procedures and guaranteeing material quality for commercial and scientific uses.

In order to fill these gaps, this work presents a thorough evaluation of $NiFe_2O_4$ nanoparticles produced by co-precipitation, explicitly comparing the as-prepared (uncalcined) and calcined (600 °C) states in terms of structural, optical, surface, and morphological properties. Also, present work offers quantitative batch-to-batch repeatability analysis that shows how reliable the synthesis procedure is, and as well offer useful information for maximizing the production of $NiFe_2O_4$ nanoparticles and guide the choice of thermal treatment parameters for particular uses.

## 2. Experimental Methods

### *2.1 Chemicals and Materials*

Commercial suppliers provided sodium hydroxide (NaOH, ≥98% purity), iron (III) chloride hexahydrate ($FeCl_3 \cdot 6H_2O$, ≥99% purity), and nickel sulfate hexahydrate ($NiSO_4 \cdot 6H_2O$, ≥99% purity). Every step of the

*Corresponding Author:sharadaadik4@gmail.com(Sharada Navnath Adik)

https://doi.org/10.30799/jnst.S101.26110201

synthesis and washing process involved the use of deionized water. Every reagent was used exactly as supplied, requiring no additional purification.

### 2.2 Co-precipitation Synthesis Protocol

Co-precipitation of nickel and iron precursors in a stoichiometric molar ratio of Ni:Fe = 1:2 was used to create $NiFe_2O_4$ nanoparticles. In short, separate aqueous precursor solutions were prepared by dissolving $NiSO_4 \cdot 6H_2O$ and $FeCl_3 \cdot 6H_2O$ in deionized water.

These solutions were then combined to create a homogenous mixed-metal salt solution. Under constant magnetic stirring (606.67 ± 11.55 rpm), the reaction mixture was kept at 80 °C. To precipitate mixed metal hydroxides, aqueous NaOH was added dropwise at a regulated addition rate (1.03 ± 0.06 mL/min). To guarantee full precipitation, the pH was adjusted and kept at 10.13 ± 0.06. To enable particle maturation and encourage hydroxide-to-oxide conversion, the suspension was aged at 80 °C for 30.67 ± 1.15 minutes after attaining the desired pH. Centrifugation was used to gather the precipitate, which was then repeatedly cleaned with deionized water to get rid of any remaining salts and soluble contaminants. A dried powder (2.06 ± 0.02 g per batch) with a yield percentage of 82.27 ± 0.83% was obtained by drying the washed precipitate at 80 °C for 12 hours. The dried powder was split into two parts: the first part was kept as the uncalcined, as-prepared sample, and the second part was calcined in a muffle furnace at 600 °C for four hours in air at a heating rate of 2 °C per minute to produce the calcined $NiFe_2O_4$ sample.

### 2.3 Characterization Methods

Phase identification and crystallographic studies were performed using powder X-ray diffraction (XRD). Cu Kα radiation (λ = 1.5406 Å) was used to record diffraction patterns. The Scherrer equation ($D = K\lambda / (\beta \cos\theta)$), where K is the shape factor (0.94), λ is the X-ray wavelength, β is the full width at half maximum (FWHM, in radians), and θ is the Bragg angle, was used to get the average crystallite size (D) [7, 8]. An integration-based method was used to calculate the crystallinity index (Xc):

$$Xc\ (\%) = (Area\_crystalline / Area\_total) \times 100$$

Brunauer-Emmett-Teller (BET) nitrogen adsorption at 77 K was used to calculate specific surface area (SSA).

Diffuse reflectance spectroscopy (DRS) was recorded over the UV-visible range to evaluate optical properties. The optical band gap (Eg) was estimated using the Tauc relation, $(\alpha h\nu)^2 = B(h\nu - Eg)$, where α is the absorption coefficient, h is Planck's constant, ν is photon frequency, and B is a proportionality constant. Urbach energy (Eu) was obtained from the exponential absorption edge by fitting the linear region of ln(α) versus photon energy (hν) in the sub-band-gap region, where the inverse slope corresponds to Eu.

Scanning electron microscopy (SEM) was used to examine particle morphology and size distribution. Approximately 200 particles were measured from SEM micrographs using image analysis software, and particle size was reported as the equivalent circular diameter.

### 2.4 Reproducibility Assessment

Fig. 1 shows schematic flow diagram of the co-precipitation synthesis process for $NiFe_2O_4$ nanoparticles. The synthesis was carried out in several batches under ostensibly identical conditions in order to evaluate batch-to-batch repeatability. Along with outcome metrics (mass of dried powder and percentage yield), important process parameters (reaction temperature, stirring speed, NaOH addition rate, final pH, aging duration, drying conditions, and calcination conditions) were recorded for each batch. Descriptive statistics (mean, standard deviation, minimum, and maximum) were used to summarize reproducibility across batches.

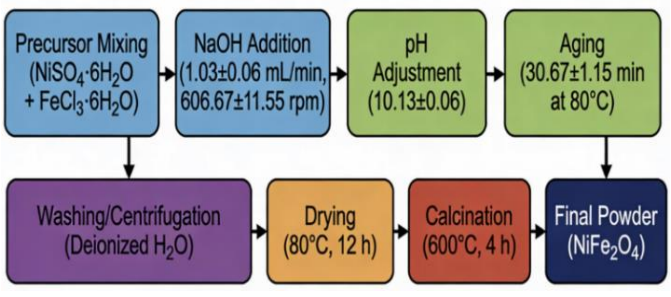


**Fig. 1** Schematic flow diagram of the co-precipitation synthesis process for $NiFe_2O_4$ nanoparticles. The workflow illustrates eight sequential steps from precursor mixing to final calcined powder, with key process parameters indicated for each stage

https://doi.org/10.30799/jnst.S101.26110201

## 3. Results and Discussion

Table 1 summarizes comparative structural data. Both the as-prepared and calcined samples showed the distinctive inverse spinel cubic crystal structure of $NiFe_2O_4$, according to XRD examination [9, 10]. The as-prepared (uncalcined) sample had a crystallinity index of 70.0% with an average XRD crystallite size of 6.50 nm. The crystallite size slightly rose to 7.14 nm (9.8% increase) and the crystallinity improved to 73.9% (5.6% relative increase) after calcination at 600 °C for four hours. These patterns align with enhanced long-range crystallographic order after heat treatment and thermal-induced grain development [11, 3]. The provided differences are descriptive observations rather than statistically tested comparisons because each condition (as-prepared and calcined) is represented by a single measurement (n = 1).

**Table 1** Comparative characterization of $NiFe_2O_4$ nanoparticles by sample condition

| Sample condition | D_XRD (nm) | Xc (%) | SSA ($m^2/g$) | Eg (eV) | Eu (eV) |
|---|---|---|---|---|---|
| As-prepared (uncalcined) | 6.5 | 70 | 174 | 1.76 | 0.3 |
| Calcined at 600 °C | 7.14 | 73.9 | 156 | 1.82 | 0.24 |
| Total | 6.82 | 71.95 | 165 | 1.79 | 0.27 |

*Note: D_XRD = XRD crystallite size (Scherrer equation); Xc = Crystallinity index (integration method); SSA = Specific surface area (BET analysis); Eg = Optical band gap (Tauc plot); Eu = Urbach energy* (disorder measure)

### 3.1 Analysis of Surface Area

After calcination, the specific surface area (SSA) dropped by 10.3%, from 174 $m^2/g$ (as-prepared) to 156 $m^2/g$ (calcined at 600 °C). This decrease is anticipated and frequently seen in nanomaterials that undergo heat treatment. The decline is caused by partial necking and agglomeration of nanoparticles at high temperatures, as well as crystallite coarsening, which is shown by the increase in D_XRD from 6.50 to 7.14 nm [11, 3]. The post-calcination SSA of 156 $m^2/g$ is still significant and consistent with real nanomaterials despite this decrease [12].

### 3.2 Optical Characteristics: Urbach Energy and Band Gap

Table 1 displays optical characterization data. An optical band gap of 1.76 eV for the as-prepared sample and 1.82 eV for the sample calcined at 600 °C, indicating a 3.4% increase, was obtained by analyzing diffuse reflectance spectra using the Tauc plot method (detailed parameters given in Table 5). An excellent linear connection in the chosen spectral region was indicated by the linear regression parameters for the Tauc plot fit of the calcined sample, which were intercept (a) = −72.80, slope (b) = 40.00, and $R^2$ = 1.00 as shown in Fig. 2.

Notable is the 20% drop in Urbach energy from 0.30 eV (as-prepared) to 0.24 eV (calcined at 600 °C). Lower values of Urbach energy indicate fewer localized defect states and less disorder. It measures the breadth of sub-band-gap states that contribute to the exponential absorption tail [13]. Thermal treatment successfully lowers fault density and enhances electronic quality, as seen by the decrease in Eu after calcination [5, 6].

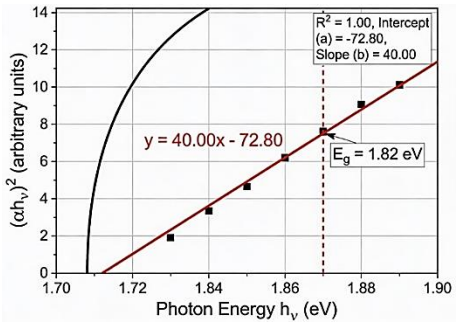


**Fig. 2** Tauc plot of $NiFe_2O_4$ nanoparticles, calcined at 600 °C

### 3.3 SEM Particle Size and Morphology

Tables 2 and 3 exhibit extensive size distribution data obtained from SEM investigation (Fig. 3) of 200 particles. With a standard deviation of 2.05 nm and a range of 6-14 nm, the descriptive statistics reveal a mean particle diameter of 9.0 nm, a median of 8.0 nm, and a mode of 8.0 nm. Mild positive (right) skewness is indicated by a mean that is somewhat higher than the median. The vast majority of particles are clustered in small size ranges 70% of particles fall within the 7-11 nm range, with the biggest single fraction (40%) in the 7-9 nm bin. 15% of the particles are smaller (5-7 nm), but bigger populations are less common. During co-precipitation, successful homogenous nucleation and growth are indicated by this narrow, concentrated distribution [3, 4, 15].

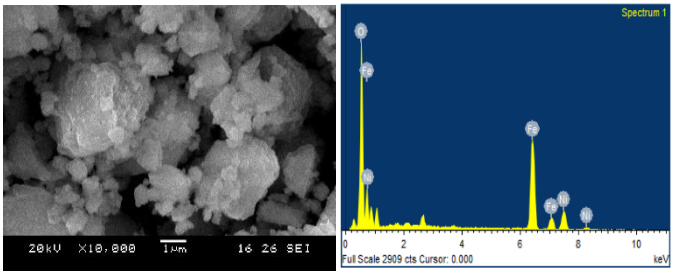


**Fig. 3** SEM image and EDS analysis spectrum of $NiFe_2O_4$ nanoparticles

**Table 2** Descriptive statistics of $NiFe_2O_4$ particle size from SEM (n = 200)

| Statistic | Value |
|---|---|
| Number of particles (n) | 200 |
| Mean size (nm) | 9 |
| Median size (nm) | 8 |
| Mode (nm) | 8 |
| Standard deviation (nm) | 2.05 |
| Minimum (nm) | 6 |
| Maximum (nm) | 14 |

*Note: n = 200 particles manually measured from SEM micrographs; Mean > Median (9.0 > 8.0) - Mild positive skewness; SD = 2.05 nm - Moderate dispersion, narrow nanometric range; Mode = 8.0 nm - Most frequent size*

**Table 3** Frequency distribution of $NiFe_2O_4$ particle size classes from SEM (n = 200)

| Size range (nm) | Number of particles | Percent of total (%) |
|---|---|---|
| 05-Jul | 30 | 15 |
| 07-Sep | 80 | 40 |
| 09-Nov | 60 | 30 |
| Nov-13 | 20 | 10 |
| 13-15 | 10 | 5 |

### *3.4 XRD Crystallite Size and SEM Particle Size Comparison*

Comparing XRD crystallite size (D_XRD = 6.50 nm for as-prepared; 7.14 nm for calcined) with SEM mean particle diameter (9.0 nm) reveals a significant finding. The XRD crystallite size (6.5-7.14 nm), calculated from Fig. 4, is less than the SEM particle size (9.0 nm), indicating that the individual particles found by SEM are probably agglomerates or polycrystalline aggregates made up of several smaller crystallites. The finding that specific surface area is more than would be predicted for perfect, non-porous spheres with a diameter of 9 nm lends credence to this interpretation. This suggests that loosely agglomerated nanocrystallite assemblies have significant interior porosity or surface roughness. Fig. 5 shows the XRD pattern of $NiFe_2O_4$ nanoparticles with/without calcination at 600 °C.

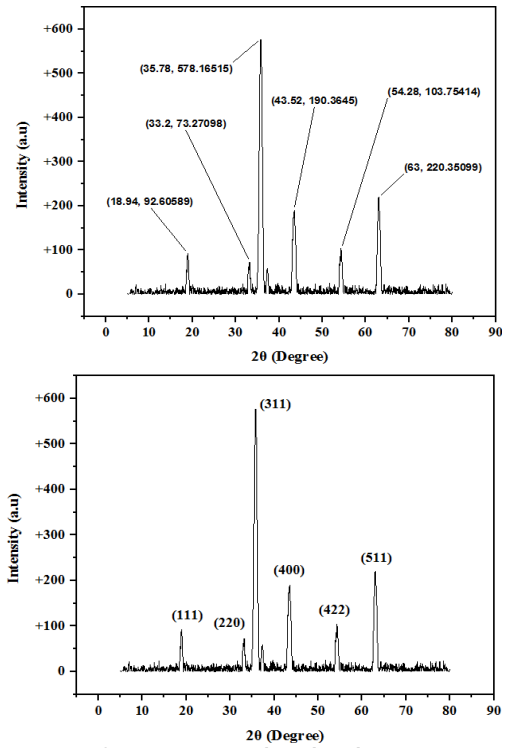


**Fig. 4** XRD spectrum of $NiFe_2O_4$ nanoparticles, calcined at 600 °C

https://doi.org/10.30799/jnst.S101.26110201

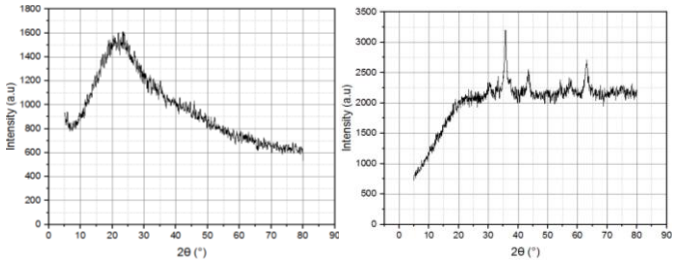


**Fig. 5** XRD pattern of $NiFe_2O_4$ nanoparticles a) without calcination and b) with calcination at 600 °C

### *3.5 Batch to Batch Reproducibility*

Table 4 summarizes the constancy of synthesis parameters throughout several batches. Precise experimental control was confirmed by the zero-standard deviation of the fixed parameters (reaction temperature, drying temperature, drying duration, calcination temperature, and calcination time). Stirring speed averaged 606.67 ± 11.55 rpm, NaOH addition rate averaged 1.03 ± 0.06 mL/min, final pH averaged 10.13 ± 0.06, and aging time averaged 30.67 ± 1.15 minutes, all of which showed slight operational variability. These slight differences are typical of real-world operating variability [3, 4]. Crucially, the product yield was very consistent: the average mass of dried powder was 2.06 ± 0.02 g (coefficient of variation 1.0%), and the average percentage yield was 82.27 ± 0.83% (coefficient of variation 1.0%). These narrow ranges show that the final material quantity and yield were not significantly impacted by minor operational variability.

**Table 4** Batch-to-batch reproducibility of synthesis parameters

| Parameter | Mean | SD | Minimum | Maximum |
|---|---|---|---|---|
| Reaction temperature (°C) | 80 | 0 | 80 | 80 |
| Stirring speed (rpm) | 606.67 | 11.55 | 600 | 620 |
| NaOH addition rate (mL/min) | 1.03 | 0.06 | 1 | 1.1 |
| Final pH | 10.13 | 0.06 | 10.1 | 10.2 |
| Aging time (min) | 30.67 | 1.15 | 30 | 32 |
| Drying temperature (°C) | 80 | 0 | 80 | 80 |
| Drying time (h) | 12 | 0 | 12 | 12 |
| Calcination temperature (°C) | 600 | 0 | 600 | 600 |
| Calcination time (h) | 4 | 0 | 4 | 4 |
| Mass of dried powder (g) | 2.06 | 0.02 | 2.04 | 2.08 |
| Percentage yield (%) | 82.27 | 0.83 | 81.6 | 83.2 |

*Note: SD = 0.00 for 6 parameters - Perfectly controlled (fixed values); Yield CV = 1.0% (82.27 ± 0.83%) - Excellent reproducibility; n ≥ 3 batches (inferred from range data)*

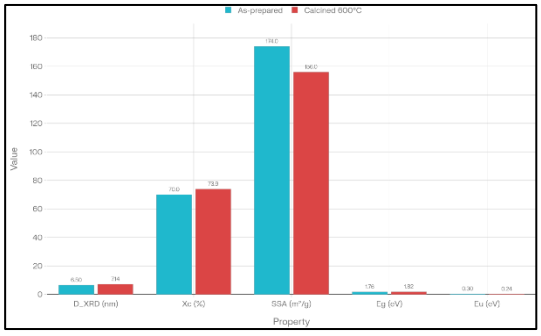


**Fig. 6** Comparative physicochemical properties of $NiFe_2O_4$ nanoparticles: as-prepared (uncalcined) versus calcined at 600°C. Five grouped bar charts show XRD crystallite size (D_XRD), crystallinity index (Xc), specific surface area (SSA), optical band gap (Eg), and Urbach energy (Eu). Light blue bars represent as-prepared samples; coral bars represent calcined samples

### *3.6 Structural and Thermal Effects Calcination*

The increase in the crystallinity index from 70.0% to 73.9% (Fig. 6) shows that calcination at 600 °C resulted in quantifiable improvements in long-range crystallographic order. Thermally-driven elimination of structural flaws and completion of crystal nucleation are responsible for this slight but steady improvement [11, 3]. Thermal grain development, a known phenomenon in nanomaterial's exposed to high temperatures, is consistent with the equivalent 9.8% rise in XRD crystallite size (6.50 to 7.14 nm) [11, 3]. Crystallite coarsening and partial sintering/ agglomeration naturally result in the concurrent 10.3% decrease in specific surface area (174 to 156 $m^2/g$) [3, 12]. This trade-off between surface area and crystallinity/crystallite size is common in calcined nanomaterials and highlights a significant optimization challenge:

applications that require maximum magnetic performance may favour higher temperatures, while those that prioritize catalytic activity may benefit from lower-temperature calcination.

### *3.7 Electronic Structure and Optical Properties*

The little but significant rise in the optical band gap after calcination (3.4% increase) from 1.76 to 1.82 eV (Fig. 7) may be caused by a number of mechanisms: (i) particle size effects, however quantum confinement effects are minimal due to the comparatively large dimensions (~9 nm) [16,17] (ii) defect-related effects, where the effective band gap increases due to the lowering of mid-gap trap states [16,17] and (iii) alterations to the electronic structure caused by thermal-induced cation reordering within the inverse spinel structure. The more important optical result is a 20% decrease in Urbach energy (0.30 to 0.24 eV). The drop in Urbach energy, which measures electronic disorder directly, shows that calcination successfully lowers the concentration of point defects, vacancies, and impurity states [15, 16]. Concurrent increases in XRD crystallinity (70.0% to 73.9%) and crystallite size (6.50 to 7.14 nm), which both lead to a more thermodynamically stable, better-ordered crystal structure with fewer flaws, provide compelling evidence for this conclusion. The resultant material has more consistent optical characteristics and sharper electronic band edges [13, 14].

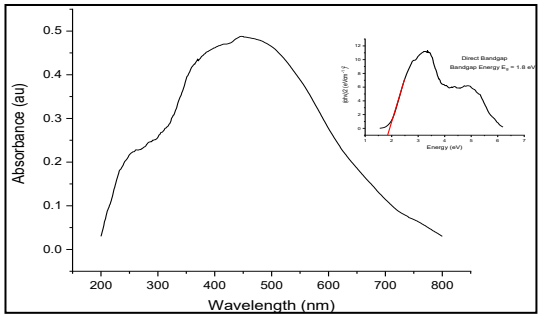


**Fig. 7** DRS Spectrum of $NiFe_2O_4$ nanoparticles

### *3.8 Nanoscale Architecture and Particle Size Distribution*

Co-precipitation produced remarkable uniformity in primary particle generation, as evidenced by the narrow, concentrated SEM particle size distribution with a mean of 9.0 nm and 70% of particles in the 7-11 nm range (Fig. 8) [3, 4, 17]. A tiny population of bigger particles (up to 14 nm) and a minor positive skewness indicate either mild agglomeration during the aging stage or minimal Ostwald ripening. Nonetheless, the fact that 85% of particles are smaller than 11 nm suggests that growth activities were successfully inhibited throughout the synthesis window. The difference between SEM particle diameter (9.0 nm) and XRD crystallite size (6.5-7.14 nm) sheds light on the material architecture: particles seen by SEM are probably secondary aggregates or weakly connected clusters of parent crystallites. Co-precipitated nanomaterials frequently have this structural characteristic. Significant internal porosity or surface roughness is qualitatively consistent with the higher-than-expected specific surface area (174 $m^2/g$). Applications needing the easy delivery of reactants to surface sites may benefit from this mesoporosity [3, 12].

The co-precipitation protocol is intrinsically reliable and scalable, as demonstrated by the quantitative repeatability data (Table 2) [3, 4]. Despite slight differences in aging time, pH, and stirring speed, the yield of 82.27 ± 0.83% was consistent across batches, indicating that the synthetic technique is tolerant of small operational fluctuations common in laboratory and semi-industrial environments [3, 4].

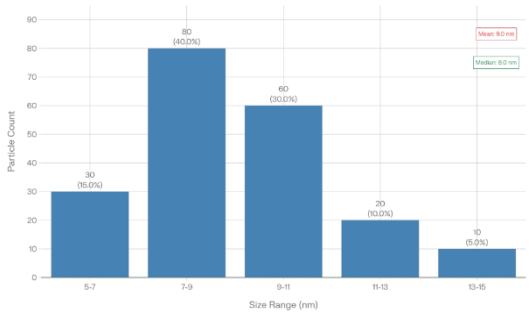


**Fig. 8** Frequency distribution histogram of $NiFe_2O_4$ particle sizes from SEM measurements (n=200). Particle size ranges are shown on the x-axis (5-15 nm in 2 nm bins), with the number and percentage of particles in each bin on the y-axis. Vertical dashed lines indicate the mean (9.0 nm, red) and median (8.0 nm, blue) particle sizes

https://doi.org/10.30799/jnst.S101.26110201

The self-limiting character of co-precipitation kinetics is probably reflected in this robustness. Precipitation accelerates and becomes comparatively insensitive to further gradual increases in pH or stirring speed until pH rises above about 9-10. The set temperatures-80 °C for reaction, 80 °C for drying, and 600 °C for calcination-represent crucial variables that need to be closely monitored. While slight changes in stirring speed, addition rate, and aging time may have an impact on the finer points of nucleation kinetics, they have little effect on overall yield or final material qualities, which is advantageous for routine manufacturing.

### *3.9 Limitations of This Study*

There are a number of significant limitations to this study: (i) *Single replicates per condition*: Inferential statistical analysis is not possible because each of the as-prepared and calcined conditions is represented by n = 1 measurement. (ii) *Missing experimental details*: There is a lack of information regarding instrument models, XRD scan parameters, SEM accelerating voltage, and other methodological requirements. (iii) *Restricted temperature range for calcination*: Only 600 °C was examined. A more comprehensive understanding of thermal impacts would result from a comparative analysis of various temperatures. (iv) *Absence of magnetic characterisation*: Comprehensive material characterisation was limited since ferrimagnetic characteristics were not measured.

## 5. Conclusion

This study shows that co-precipitation is a scalable, dependable, and efficient way to create $NiFe_2O_4$ nanoparticles with tunable structural and optical features and good batch-to-batch repeatability. While retaining nanometric dimensions and a reasonable specific surface area (156 $m^2/g$), calcination at 600 °C results in slight but significant improvements in crystallinity (70.0% to 73.9%), crystallite size (6.50 to 7.14 nm), and electronic quality (Urbach energy 0.30 to 0.24 eV). Subtle optical adjustments (band gap 1.76 to 1.82 eV) accompany these advancements. SEM examination demonstrated successful homogeneous nucleation and growth, confirming homogenous particle shape with a mean diameter of 9.0 nm and 70% of particles in the narrow 7-11 nm range. The protocol's applicability for research-scale and possibly larger production contexts was confirmed by the quantitative repeatability assessment, which showed synthesis yields of 82.27 ± 0.83% with strict parameter control.

In order to improve size control and achieve even narrower particle size distributions, future research should examine: (i) a greater range of calcination temperatures; (ii) detailed magnetic characterization (magnetometry, Mössbauer spectroscopy); (iii) catalytic activity testing; and (iv) systematic variation of synthesis pH and aging time. This co-precipitated $NiFe_2O_4$ material is a promising candidate for applications in magnetic devices, catalytic systems, gas sensors, and other technologies requiring dependable, high-performance ferrimagnetic nanocrystals because of its high synthesis reproducibility, controllable nanoscale dimensions, improved structural order, and decreased electronic disorder.

## References

[1] H. Guo, A.S. Barnard, Thermodynamic modelling of nanomorphologies of hematite and goethite, J. Mater. Chem. 21 (2011) 11566–11577.
[2] B.D. Cullity, C.D. Graham, Introduction to magnetic materials, 2nd Ed., Hoboken, Wiley-IEEE Press, NJ, USA, 2009.
[3] R. Jitesh, S. Khan, R. Patel, Synthesis and study of the properties of metal oxides using chemical co-precipitation, J. Nanosci. Nanotechnol. 1(2) (2024) 108-125.
[4] A.K. Tiwar, M. Kumar, S. Singh, Controlled synthesis of metal oxide nanoparticles: a comprehensive review, Nanoscale. 15(18) (2023) 8035-8072.
[5] P. Makuła, M. Pacia, W. Macyk, How to correctly determine the band gap energy of modified semiconductor photocatalysts based on UV-vis spectra, J. Phys. Chem. Lett. 9(23) (2018) 6814-6817.
[6] C. Kaiser, M.C. Schulze, B.A. Gregg, A universal Urbach rule for disordered organic semiconductors, Nat. Mater. 20(8) (2021) 1068-1073.
[7] R. Rotaru, M. Savin, N. Tudorachi et al., XRD analysis and crystallinity determination, supplementary data for ferromagnetic iron oxide–cellulose nanocomposites prepared by ultrasonication, Polym. Chem. 8(47) (2017) 7306-7315.
[8] InstaNANO, Percent crystallinity calculator from XRD (X-ray Diffraction). Available from: https://instanano.com/all/characterization/xrd/percent-crystallinity/ (Accessed on: 26.01.2026)
[9] O.A. Restrepo, O. Arnache, N. Mousseau, An approach to understanding the formation mechanism of $NiFe_2O_4$ inverse spinel, Materialia 33 (2024) 102031.
[10] S.R. Shahina, S. Vidya, Synthesis, structural and dielectric characterization of $NiFe_2O_4$ nanoparticles, AIP Conf. Proc. 2379(1) (2021) 030012.
[11] C.T. Campbell, Catalyst-support interactions: electronic perturbations, Nat. Chem. 4(8) (2012) 597-598.

[12] S. Brunauer, P.H. Emmett, E. Teller, Adsorption of gases in multimolecular layers, J. Am. Chem. Soc. 60(2) (1938) 309-319.
[13] F. Urbach, The long-wavelength edge of photographic sensitivity and of the electronic absorption of solids, Phys. Rev. 92(5) (1953) 1324.
[14] M. Piccardo, L. Martinelli, C.K. Li, Y.R. Wu, J.S. Spec, R.M. Farrell et al., Localization landscape theory of disorder in semiconductors II. Urbach tails in disordered quantum layers, Phys. Rev. B 95(14) (2017) 144205.
[15] P. Srivastava, P.S. Gour, Synthesis and Characterization of $NiFe_2O_4$ Nanoparticles: Structural and Optical Insights, Int. J. Innov. Res. Growth 13(4) (2024) 103.
[16] Shimadzu, Band gap determination from diffuse reflectance spectra: Tauc Plot Method, Appl. Note A428 (2020) 1-3.
[17] J. Tauc, Optical properties and electronic structure of amorphous semiconductors, In: Mort J, Pai DM, Editors, Optical effects in amorphous semiconductors, Academic Press, New York, 1979, pp.159-220.

***This article is published as part of the Special Issue*** *on*
"National Conference on Recent Interdisciplinary Approaches in Allied Sciences, Humanities, Agriculture, Engineering, Law and Management"

*Issue Editor:*
Dr. B.Y. Bagul

**Special Issue Publication and Peer-Review Statement**

This article is included in the Special Issue of the journal comprising peer-reviewed papers selected from the National Conference on "Recent Interdisciplinary Approaches in Allied Sciences, Humanities, Agriculture, Engineering, Law, and Management (NCRIASHAELM–2025)", held on 24 December 2025. The conference was sponsored by Pradhan Mantri Uchchatar Shiksha Abhiyan (PM-USHA), Ministry of Education, Government of India, and convened by Dr. B. Y. Bagul, IQAC Coordinator and Head, Department of Physics, Vasantrao Naik Arts, Science and Commerce College. All manuscripts included in this Special Issue underwent editorial screening and peer review in accordance with the journal's standard review policies and ethical guidelines.

https://doi.org/10.30799/jnst.S101.26110201

*Cite this Article as:* Sharada Navnath Adik, Synthesis and characterization of nickel ferrite ($NiFe_2O_4$) nanoparticles through co-precipitation method, J. Nanosci. Tech. 11(2) (2026) 1040–1044.